

# Real-Space Visualization of Energy Loss and Carrier Diffusion in a Semiconductor Nanowire Array Using 4D Electron Microscopy

Riya Bose, Jingya Sun, Jafar I. Khan, Basamat S. Shaheen, Aniruddha Adhikari, Tien Khee Ng, Victor M. Burlakov, Manas R. Parida, Davide Priante, Alain Goriely, Boon S. Ooi, Osman M. Bakr, and Omar F. Mohammed\*

By combining the nanometer spatial resolution of electron microscopy (EM) with ultrafast electron pulses, the invention of so-called four-dimensional ultrafast electron microscopy (4D UEM) has indeed unraveled a new dimension in imaging techniques that enables the space–time visualization of non-equilibrium electronic and structural dynamics.<sup>[1–3]</sup> In a UEM experiment, single electron pulses, which are generated by femtosecond (fs) laser pulses, are utilized and further synchronized with optical-excitation pulses, providing a new, powerful methodology to image ultrafast dynamical processes in real-space and time. In this regime, the replacement of a continuous electron beam, as used in conventional EM, by photoelectron packets, for which the probe pulse contains at most a few electrons, can significantly eliminate Coulomb repulsion between electrons and allows the temporal resolution of UEM to be determined only by the optical pulse duration, while maintaining the same spatial resolution of EM.<sup>[1–4]</sup> Among the different techniques of microscopy that have been integrated into UEM,<sup>[5–10]</sup> scanning ultrafast electron microscopy (S-UEM) is particularly befitting for selectively probing surface dynamics in real-space and time.<sup>[6,11–13]</sup> More specifically, in S-UEM, time-resolved secondary electron (SE) images are generated from the specimen surface following *in situ* fs optical excitation (see Figure 1) and probing with a pulsed primary electron beam. This allows for the study of physical and chemical processes on the surface and

at the interface of materials.<sup>[6,11,12,14]</sup> Recently, ultrafast transient absorption (TA) microscopy techniques have also been developed to examine charge-carrier dynamics of nanostructures with high spatial and temporal resolutions;<sup>[15,16]</sup> however, these techniques are limited by the laser's relatively large penetration depth, and therefore they record mainly bulk information.

The ultrafast dynamics of charge carriers on materials surfaces play a pivotal role in controlling the applicability of nanoscale materials, especially for one-dimensional (1D) nanostructures, e.g., nanowires (NWs)/nanorods, which have been extensively used for electronic, optoelectronic, and photoelectrochemical applications due to their interesting and unique properties.<sup>[17–28]</sup> For instance, an understanding of nonradiative energy losses at the surface, via carrier–carrier and carrier–phonon interactions, following pulsed-laser excitation is crucial for wide bandgap semiconductors, e.g., group-III nitride materials and alloys.<sup>[29–33]</sup> Of particular interest is indium gallium nitride (InGaN), which has found wide-spread use as the active media in solid-state light-emitting diodes, laser diodes, and photovoltaic devices because of its tunable bandgap from 0.7–3.4 eV and other characteristics such as direct bandgap, high absorption coefficient, and irradiation resistance.<sup>[34–38]</sup> However, the internal quantum efficiency (IQE) of these devices is limited by an energy-loss mechanism, which leads to a decrease in the IQE at high driving currents. This phenomenon is commonly known as “efficiency droop”.<sup>[39–41]</sup> The precise nature of this energy-loss mechanism has been the subject of intense debate, and a variety of pathways have been proposed. Intra- and interband Auger recombination events, which involve the scattering of an electron within the lowest and to the second-lowest conduction bands, respectively, along with alloy scattering, i.e., the scattering of carriers due to the disorder component of the crystal potential, have been the most reported explanations.<sup>[42–46]</sup> The scattering processes also limit the mobility of charge carriers, which, in turn, diminishes the efficiency of optoelectronic devices.<sup>[46–48]</sup> It should also be noted that under low injection current density, the carrier diminishing mechanism in the InGaN nanowires is dominated by the surface-states-related Shockley–Read–Hall (SRH) recombination, a monomolecular recombination phenomenon. It has been reported that the reduction in surface states results in higher peak-IQE and overall higher IQE, or the related quantity, the external quantum efficiency, even when the Auger recombination process starts dominating at a higher

Dr. R. Bose, Dr. J. Sun, Dr. J. I. Khan, B. S. Shaheen,  
Dr. A. Adhikari, Dr. M. R. Parida,  
Prof. O. M. Bakr, Prof. O. F. Mohammed  
Solar and Photovoltaics Engineering Research Center  
Division of Physical Sciences and Engineering  
King Abdullah University of Science  
and Technology (KAUST)  
Thuwal 23955-6900, Kingdom of Saudi Arabia  
E-mail: omar.abdelsaboor@kaust.edu.sa  
  
Dr. T. K. Ng, D. Priante, Prof. B. S. Ooi  
Photonics Laboratory  
Computer, Electrical, and Mathematical Sciences  
and Engineering, KAUST  
Thuwal 23955-6900, Kingdom of Saudi Arabia  
  
Dr. V. M. Burlakov, Prof. A. Goriely  
Mathematical Institute  
University of Oxford  
Woodstock Road, Oxford OX2 6GG, UK



DOI: 10.1002/adma.201600202

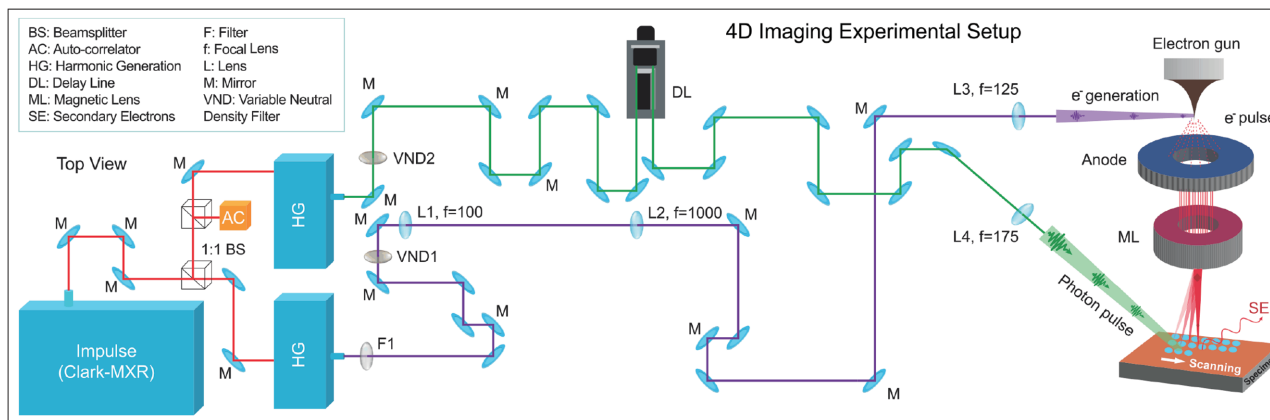


**Figure 1.** A conceptual schematic of the S-UEM. Pulsed electrons are scanned over the surface that is illuminated by an optical pulse. The emitted SEs are then detected to construct time-resolved SE images at different time delays between the optical and electron pulses. A ray diagram of the 4D S-UEM optical setup is provided in Figure S1 in the Supporting Information.

injection current density.<sup>[49]</sup> Therefore, to unlock the full potential of InGaN for efficient device-based applications, a precise knowledge of the surface recombination dynamics is of utmost importance. The limited penetration depth of the electron beam in S-UEM warrants information about charge-carrier recombination and diffusion processes dominated mostly by surface states and will indirectly shed light on the improvement of the IQE in the low-injection-current-density regime of operation.

Herein, using 4D S-UEM, we image the charge-carrier dynamics of a densely packed array of InGaN NWs, 460–510 nm in length and 20–40 nm in diameter, oriented vertically on a silicon (Si) substrate. Unlike the cases of CdSe single crystals and Si,<sup>[11]</sup> where bright contrast has been observed at positive time delays, the measured contrast in time-resolved SE images at both negative and positive time delays is dark. From the time scale obtained, we are able to deduce the deactivation channels and the mechanism of SE energy loss. Interestingly, imaging the signal spread over a time window of 6.0 nanoseconds (ns) provides clear experimental evidence for the diffusion of charge carriers across the boundaries of the nanowire array, which is indeed a critical parameter to control the efficiency of InGaN light-emitting devices and laser diodes.<sup>[50–52]</sup>

The schematic diagram of 4D S-UEM is provided in Figure 1, and detailed information on the principle of operation is published elsewhere.<sup>[11,13]</sup> Briefly, the output of an fs Clark-MXR fiber laser system is integrated to a modified Quanta FEI-650 scanning electron microscope. The laser delivers IR pulses centered at 1030 nm with a pulse width of ~270 fs and the repetition rate ranges from 200 kHz to 25.4 MHz. The fundamental output is split by a 1:1 beam splitter, and thus it simultaneously pumps two second/third-harmonic generators (Clark-MXR) to produce 515 or 343 nm pulses. The 343 nm output is directed and tightly focused onto the emitter tip, which photogenerates electron pulses that are then accelerated using 30 kV voltage. The 515 nm output enters the microscope through a viewport that is at 50° angle relative to the surface normal and is focused on the specimen for dynamics initiation. The scanning process of the electron beam takes place across the surface of the sample, both the laser excited and unexcited regions, in raster pattern, and the SEs emitted from the sample are detected by a

positively biased Everhart–Thornley detector. The SE images are obtained as integration of 64 frames with dwell time of 300 ns at each pixel to improve the signal-to-noise ratio. Finally, all experiments are conducted at a repetition rate of 8 MHz to ensure full recovery of the specimen before arrival of the next pulse.

**Figure 2** shows the time-resolved SE images that are obtained from InGaN NWs at different time delays in response to the 515 nm excitation pulse. As can be clearly seen, a dark contrast is observed in the laser-illuminated region when the electron pulse arrives before the clocking photon pulse near time zero. At positive time delays, the measured contrast is also dark, which suggests that the SEs generated in both regimes lose energy during their migration to the surface in order to escape (details described below). It should be noted that the dark contrast spreads beyond the laser footprint region with time, which originates from carrier diffusion from the laser illuminated part. Dense packing of the NW array enables carrier diffusion across the boundaries of the NWs, and for ease of understanding, the sample can be considered as a thin film with columnar growth.

To investigate the carrier dynamics, the SE intensities from the center and outside the periphery of the laser excitation footprint are plotted as a function of the time delay between optical and electron pulses (**Figure 3**, top panel). The pulse energy of the pump beam is 0.06 nJ at the sample; it is worth mentioning that we also performed the same experiment under different pulse energies (0.012, 0.036, and 0.073 nJ), and the kinetics at the laser footprint remain essentially the same, indicating the independence of the carrier dynamics for this range of pulse energy. It is worth pointing out that the Si substrate does not contribute to the observed contrast change due to the very low excitation-pulse energies used. In addition, the long length of the InGaN NWs does not allow any SEs to come out from the deeply buried Si substrate. For the SE signal collected from the center of the laser-illuminated region, it is observed that the intensity reaches its maximum darkness within the temporal resolution of the instrument. As time passes, in addition to the spreading of this dark contrast, the signal fades away, indicating carrier relaxation. It should be noted that the carrier relaxation is much slower than the maximum time window

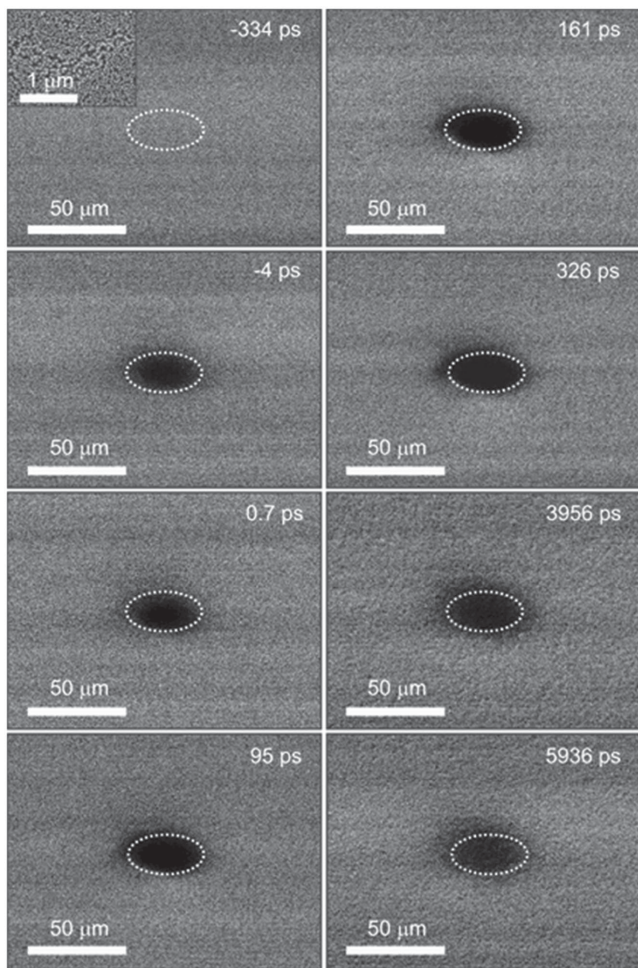


**Figure 2.** Time-resolved SE images of InGaN NWs at the indicated time delays. The dashed ellipses indicate the footprint of the clocking optical beam on the specimen ( $\approx 40 \mu\text{m}$ ). No observable change in the contrast at very negative time signifies the recovery of the system to an equilibrated state after each pump-probe event. An SEM image of the nanowires is shown in the inset (top panel) and cross-section SEM image has been provided in Figure S2 (Supporting Information).

of the S-UEM; therefore, an accurate decay time cannot be extracted from fitting the data on this time scale. On the other hand, the SE kinetics obtained from outside the periphery of the signal (approximately a few micrometers) shows a time constant of  $1.2 \pm 0.2 \text{ ns}$  to reach its maximum intensity. To confirm the origin of this slow dynamic feature, we use the ambipolar diffusion coefficient for electrons in InGaN nanowires ( $26 \text{ cm}^2 \text{ s}^{-1}$ )<sup>[11,53]</sup> to calculate the carrier diffusion/spreading away from the laser-footprint region. Based on this information, we found that carriers can diffuse  $\approx 3.95 \mu\text{m}$  within the  $6 \text{ ns}$  time window, which is in good agreement with our measurements. This observation provides clear evidence for the accessibility of probing carrier spreading on materials surfaces in real-space and time using S-UEM.

The observed dark contrast in the S-UEM images at negative delays with a  $20 \pm 4 \text{ ps}$  time constant (Figure 3, top panel; inset) can be explained as follows. In this regime, the electron pulse arrives at the sample prior to the fs optical pulse (Figure 3,

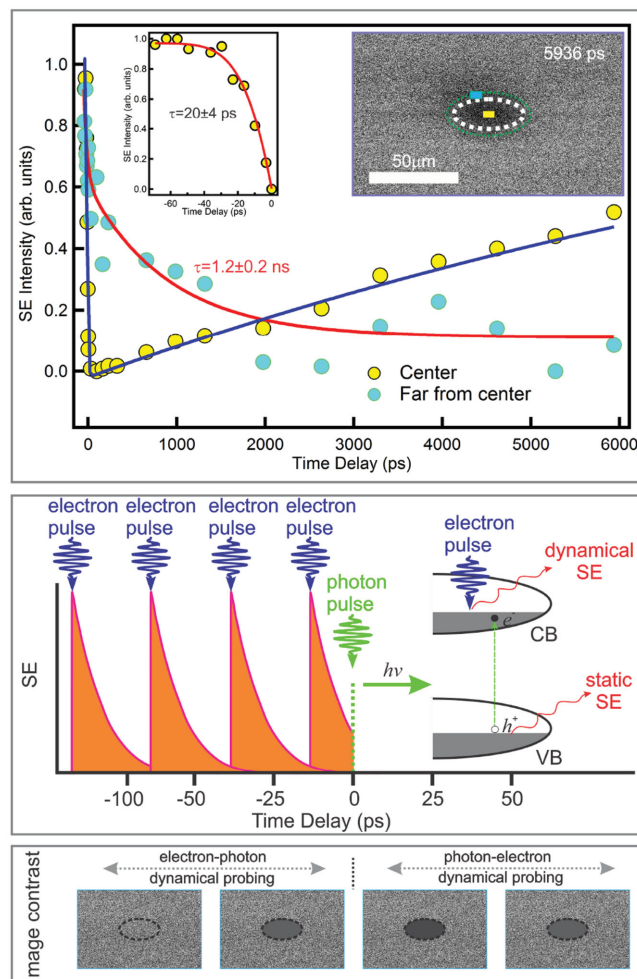


**Figure 3.** Top panel: Dynamics of the temporal evolution of SE intensity at the center and outside of the laser footprint (indicated in the SE image). Inset shows the SE kinetics in the negative time region. Middle panel: Schematic diagram showing the principle of imaging in negative (the electron pulse arriving at the sample prior to the optical pulse) and positive (the optical pulse arriving prior to the electron pulse) time scales. The bottom panel shows typical SE images obtained in the time regimes that are probed: electron–photon dynamical probing and photon–electron dynamical probing.

middle panel).<sup>[6,11,12]</sup> Thus, the non-equilibrium change in the sample by electron impact is altered again by the following optical pulse. This dark contrast can be attributed either to the diffusion of plasmon-excited carriers that are generated from deeper areas of the sample by electron impact, which are perturbed by electron–hole pairs generated by the clocking photon pulse, or to different scattering processes.<sup>[54]</sup> Considering the ambipolar diffusion coefficient of  $26 \text{ cm}^2 \text{ s}^{-1}$  in InGaN NWs, if we assume that  $\approx 250 \text{ nm}$  from the top surface of the NWs constitutes the region of distribution that can eventually contribute to the SE signal, we obtain (using  $L^2/D$ ; where  $L$  = the distance that the charge carrier diffuses and  $D$  = diffusion coefficient) a time constant of  $\approx 24 \text{ ps}$  for the plasmon excited carriers to reach the surface. This seems to be a reasonable explanation for the observed dark contrast. On the other hand, scattering seems less likely because the characteristic time constants for electron–electron and electron–phonon scattering processes are

in the range of a few femtoseconds and picoseconds, respectively, which do not match with our experimental observation. To further confirm the origin of the dark contrast in the negative time, we performed two different control S-UEM experiments, by varying the pulse energy of the electron beam as well as the thickness of the sample, both of which suggest that the negative signal must have originated from plasmon excited carriers that are generated from deeper areas of the sample (experimental details are provided in Figure S3 and S4, Supporting Information).

At positive time delays in the S-UEM experiment, the optical pulse promotes a fraction of the valence-band electrons to the conduction band (Figure 3, middle panel). Compared to the electrons in an unexcited specimen, the promoted electrons have higher probability of emitting SEs to the vacuum level when they are scattered by the energetic primary electron beam, resulting in an enhanced probability of SE emission. This should give rise to a bright contrast in the image, as has been observed for Si or CdSe.<sup>[11]</sup> However, the dark contrast observed in the case of InGaN NWs suggests a different mechanism, where SEs in the conduction band lose energy during transit to the surface and they do not reach the detector because of an energy deficit, as explained by Cho et al.<sup>[12]</sup> In this case, scattering processes with photogenerated electron-hole pairs are most likely responsible for the energy loss. As the effective cross-section for the scattering of SEs with conduction electrons is much higher than that with valence electrons,<sup>[12]</sup> a decrease in SE emission and subsequently a low, i.e., dark contrast is observed.

We further compare our S-UEM imaging results with carrier dynamics that we obtained from ultrafast pump-probe spectroscopic measurements. Figure 4A shows the TA spectra of the nanowires in the ns–μs region after 515 nm optical excitation. Clear ground-state bleach is observed around 460 and 603 nm due to the removal of the occupied valence-band population, as confirmed from the peak position of the steady-state absorption spectrum of the nanowires (Figure S5, Supporting Information). The kinetics of the ground-state bleach recovery at 464 nm (measured with ns-TA spectroscopy), as fitted with a double-exponential function, yields two time components, of  $\approx 2$  and  $\approx 101$  ns (Figure 4B, inset). The short component matches the band-edge excitonic recombination time of InGaN that has been reported in the literature.<sup>[55,56]</sup> The long component probably arises from the recombination via a localized state, where the overlap between the electron and hole wavefunctions is considerably low, or via some intrabandgap trap sites, which may arise in indium-rich regions.<sup>[57,58]</sup> When the TA kinetics is compared with the kinetics obtained from the S-UEM, it is observed that within a time window of 4 ns (Figure 4B), both kinetics are exactly the same, which clearly proves the authenticity of the data obtained from S-UEM.

To get further insight into the carrier relaxation and diffusion process, we performed numerical modeling for the SE signal variation in time and space. We assume that the sample material is homogeneous in the lateral direction, i.e., possible inhomogeneity of the physical properties is effectively averaged off. Hence the model involves effective diffusion coefficients for electrons and holes, which most likely are determined by carrier migration between individual nanowires (inter), as this process is expected to be much slower than carrier migration

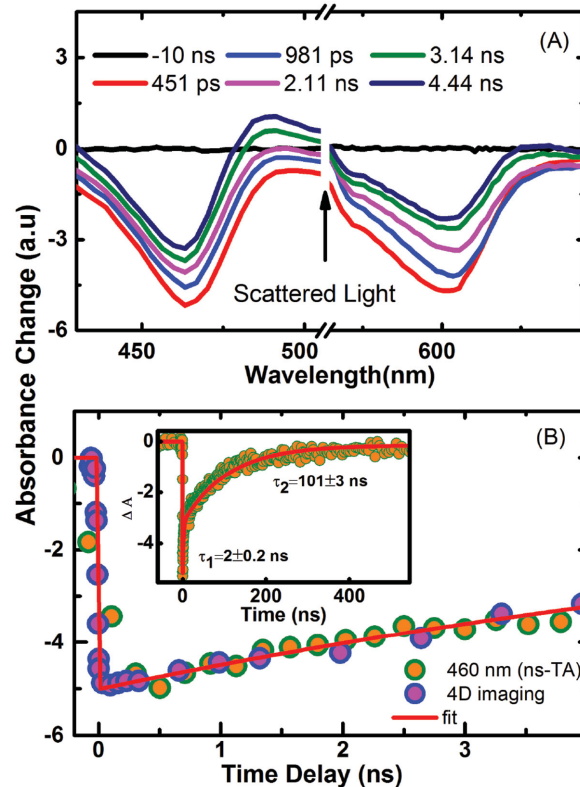


**Figure 4.** A) The TA spectra for InGaN NWs in the ns region at the indicated time delays. B) Kinetics obtained at 460 nm from the TA spectra in comparison with the kinetics obtained from the S-UEM. Both data sets overlap with each other exactly within the 4 ns time-window. Inset shows the complete kinetics for the ground state bleach recovery with a longer time window, as obtained from the TA measurement. The solid lines are the best fit for the experimental data.

inside the nanowires (intra). As the SE signal is proportional to local free-electron concentration on the surface of the materials, we take into account two main processes taking place after laser pulse excitation of the nanowires. The first process is the diffusion of the photoexcited free electrons and holes across the boundaries of the nanowires array resulting in a visible size increase of the area generating the SE signal. The second process is the recombination of free carriers resulting in the overall SE signal decrease. To simplify the task, we assume that the excited area has a circular shape and the carrier diffusion is isotropic such that we can neglect the shape variation. This also allows the diffusion problem to be reduced to a 1D one. Then, the space and time variation of the free electron and hole concentrations  $n_e$  and  $n_h$ , respectively, can be described by the following equations:

$$\begin{aligned} \frac{dn_e(x,t)}{dt} &= D_e \frac{d^2 n_e(x,t)}{dx^2} - \gamma_1 n_e(x,t) - \gamma_2 n_e(x,t) \cdot n_h(x,t) \\ \frac{dn_h(x,t)}{dt} &= D_h \frac{d^2 n_h(x,t)}{dx^2} - \gamma_1 n_h(x,t) - \gamma_2 n_e(x,t) \cdot n_h(x,t) \end{aligned} \quad (1)$$

where all concentrations are normalized to the initial concentration at its maximum,  $N_{e0}$ ;  $D_e$  and  $D_h$  are the diffusion coefficients

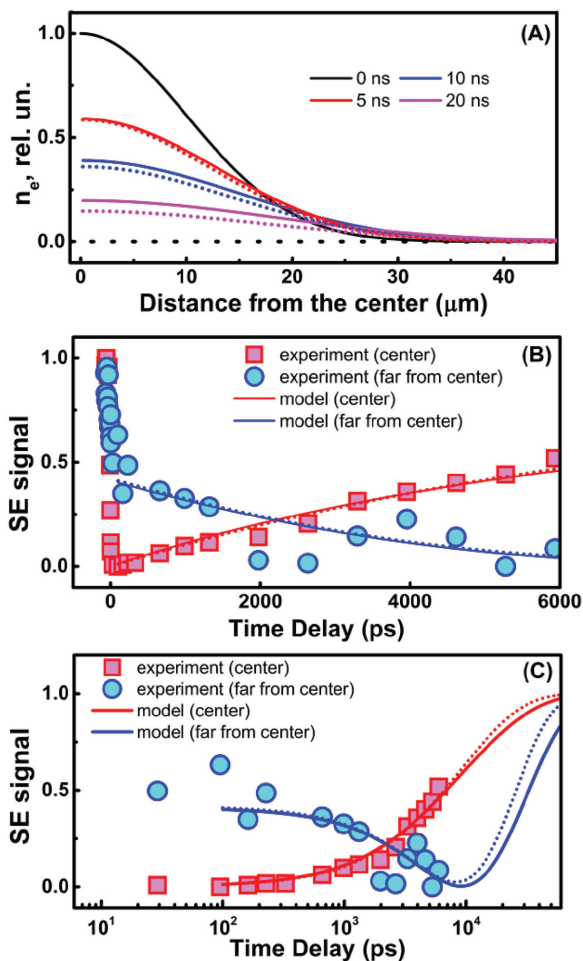


**Figure 5.** A) Distribution of electronic concentration at different time moments. B) Numerical fit for the kinetics of SE intensity evolution at the center and outside of laser footprint obtained by simulation. C) Numerical fit for the kinetics of SE intensity evolution at extended time scale from the center and outside of laser footprint obtained by simulation. The model parameters used for simulation are  $D_e = D_h = 45 \text{ cm}^2 \text{ s}^{-1}$ ,  $\gamma_1 = 4 \times 10^7 \text{ s}^{-1}$  ( $\gamma_1 = 7 \times 10^7 \text{ s}^{-1}$  for dotted lines),  $\gamma_2 = 4 \times 10^7 \text{ s}^{-1}$  ( $\gamma_2 = 0$  for dotted lines).

of electrons and holes, respectively;  $\gamma_1$  and  $\gamma_2$  are monomolecular and bimolecular recombination rates, respectively. Both these rates have dimensionality of  $\text{s}^{-1}$ . To translate  $\gamma_2$  to the common dimensionality of  $\text{cm}^3 \text{ s}^{-1}$ , it has to be divided by  $N_{e0}$ . The latter can be estimated using the excitation pulse energy, the pulse cross-section, and the material absorption coefficient.

Equation (1) has been solved numerically with the initial carrier distributions  $n_e(x,0) = n_h(x,0) = \exp(-x^2/2\sigma^2)$  with the distribution half width  $\sigma = 10^{-3} \text{ cm}$  for various values of the parameters  $D_e$ ,  $D_h$ ,  $\gamma_1$ , and  $\gamma_2$  to fit the experimental data for normalized SE signal in the center and at the edge of the excited area (see Figure 5A). The normalized simulated signal at the center ( $x = 0$ ) has been taken as  $1 - n_e(0,t)$ , while at the edge (at the distance  $x = 2.5\sigma$  from the center) it is proportional to  $1 - \alpha n_e(2.5\sigma,t)$  with  $\alpha$  being the fitting parameter. We found that for the parameter values  $D_e = 45 \text{ cm}^2 \text{ s}^{-1}$ ,  $\gamma_1 = 7 \times 10^7 \text{ s}^{-1}$ , and  $\gamma_2 \approx 0$ , the best fit (shown by solid lines in Figure 5B) for

both SE signals (at  $x = 0$  and  $x = 2.5\sigma$ ) can be obtained, suggesting that holes are not taking part in the SE signals. It is worth pointing out that a fit of nearly similar quality (see solid lines in Figure 5B) can be obtained for the values  $\gamma_1 = \gamma_2 = 4 \times 10^7 \text{ s}^{-1}$  and  $D_e = D_h = 45 \text{ cm}^2 \text{ s}^{-1}$  suggesting that the simulation results are not very sensitive to the presence of bimolecular recombination and the presence of holes, which again implies that the modeling results would not be sensitive also to the triple-molecular electronic relaxation, i.e., the Auger processes. Therefore, we can conclude that the leading mechanism of nonradiative energy loss involves monomolecular electronic relaxation, i.e., surface-states-related SRH recombination. The higher value of the electronic diffusion coefficient  $D_e$  compared to that used above ( $26 \text{ cm}^2 \text{ s}^{-1}$ ) is due to the presence of recombination. The overall decrease in electronic density due to recombination requires a much higher value of  $D_e$  to account for the same increase in the SE signal at the periphery region as in the case without the recombination. This is illustrated in Figure 5A by the decreasing and broadening distribution of electronic density. The presence of recombination is really necessary for reproducing the experimental shape of the SE signal in the center (red lines in Figure 5B). To summarize, the model provides a good description of the SE signals in both of the experimentally measured spatial regions, i.e., in the center and at the periphery of the laser spot (see Figure 5B). This description allows rather accurate estimation of the electron diffusion coefficient while the description quality is not very sensitive to all the other parameters, as their cumulative effect is mutually compensated (compare the solid and dotted lines in Figure 5B,C).

In conclusion, we report first real-space imaging of the charge-carrier dynamics on the surface of InGaN NWs using 4D S-UEM. This technique provides the unique opportunity to directly visualize surface dynamics selectively, including carrier recombination and diffusion in real-space and time, thus providing access to a territory that is beyond the reach of either static electron imaging or time-resolved laser spectroscopy/microscopy. Moreover, we identify the possible deactivation channels and the mechanism of secondary electron energy loss in the system. Numerical modeling for the SE signal variation in time and space further gives an accurate estimation of the carrier relaxation and diffusion process, which is consistent with the experimental results. Thus, real-time visualization of the charge-carrier dynamics on the surface not only provides a basic understanding of semiconductor physics but also enables intricate mapping of energy loss pathways, which are major hurdles for advancing the performance of InGaN based optoelectronic devices.<sup>[59,60]</sup>

## Supporting Information

Supporting Information is available from the Wiley Online Library or from the author.

## Acknowledgements

R.B. and J.S. contributed equally to this work. The work was supported by the King Abdullah University of Science and Technology (KAUST)

and King Abdulaziz City for Science and Technology TIC (Technology Innovation Center) for Solid-State Lighting at KAUST. T.K.N. and B.S.O. gratefully acknowledge contribution from Pallab Bhattacharya, University of Michigan, USA. T.K.N. and D.P. gratefully acknowledge Rami T. Elafandy (Photonics Laboratory, KAUST) for the effort and assistance in scanning electron microscopy experiments. The authors declare no competing financial interests.

Received: January 13, 2016

Revised: February 28, 2016

Published online: April 25, 2016

- [1] D. J. Flannigan, A. H. Zewail, *Acc. Chem. Res.* **2012**, *45*, 1828.
- [2] A. H. Zewail, *Science* **2010**, *328*, 187.
- [3] V. A. Lobastov, R. Srinivasan, A. H. Zewail, *Proc. Natl. Acad. Sci. USA* **2005**, *102*, 7069.
- [4] H. Petek, *ACS Nano* **2014**, *8*, 5.
- [5] H. S. Park, J. S. Baskin, O.-H. Kwon, A. H. Zewail, *Nano Lett.* **2007**, *7*, 2545.
- [6] D.-S. Yang, O. F. Mohammed, A. H. Zewail, *Proc. Natl. Acad. Sci. USA* **2010**, *107*, 14993.
- [7] M. S. Grinolds, V. A. Lobastov, J. Weissenrieder, A. H. Zewail, *Proc. Natl. Acad. Sci. USA* **2006**, *103*, 18427.
- [8] A. Yurtsever, A. H. Zewail, *Science* **2009**, *326*, 708.
- [9] F. Carbone, O.-H. Kwon, A. H. Zewail, *Science* **2009**, *325*, 181.
- [10] O.-H. Kwon, A. H. Zewail, *Science* **2010**, *328*, 1668.
- [11] O. F. Mohammed, D.-S. Yang, S. K. Pal, A. H. Zewail, *J. Am. Chem. Soc.* **2011**, *133*, 7708.
- [12] J. Cho, T. Y. Hwang, A. H. Zewail, *Proc. Natl. Acad. Sci. USA* **2014**, *111*, 2094.
- [13] J. Sun, V. A. Melnikov, J. I. Khan, O. F. Mohammed, *J. Phys. Chem. Lett.* **2015**, *6*, 3884.
- [14] E. Najafi, T. D. Scarborough, J. Tang, A. Zewail, *Science* **2015**, *347*, 164.
- [15] E. M. Grumstrup, M. M. Gabriel, E. M. Cating, C. W. Pinion, J. D. Christesen, J. R. Kirschbrown, E. L. Vallorz, J. F. Cahoon, J. M. Papanikolas, *J. Phys. Chem. C* **2014**, *118*, 8634.
- [16] M. M. Gabriel, J. R. Kirschbrown, J. D. Christesen, C. W. Pinion, D. F. Zigler, E. M. Grumstrup, B. P. Mehl, E. E. M. Cating, J. F. Cahoon, J. M. Papanikolas, *Nano Lett.* **2013**, *13*, 1336.
- [17] A. Salant, M. Shalom, Z. Tachan, S. Buhbut, A. Zaban, U. Banin, *Nano Lett.* **2012**, *12*, 2095.
- [18] M. T. McDowell, S. W. Lee, I. Ryu, H. Wu, W. D. Nix, J. W. Choi, Y. Cui, *Nano Lett.* **2011**, *11*, 4018.
- [19] C. K. Chan, R. N. Patel, M. J. O'Connell, B. A. Korgel, Y. Cui, *ACS Nano* **2010**, *4*, 1443.
- [20] Y. M. Zuev, J. S. Lee, C. Gallo, H. Park, P. Kim, *Nano Lett.* **2010**, *10*, 3037.
- [21] L. Venkataraman, Y. S. Hong, P. Kim, *Phys. Rev. Lett.* **2006**, *96*, 076601.
- [22] T. A. Su, H. Li, V. Zhang, M. Neupane, A. Batra, R. S. Klausen, B. Kumar, M. L. Steigerwald, L. Venkataraman, C. Nuckolls, *J. Am. Chem. Soc.* **2015**, *137*, 12400.
- [23] Y.-J. Doh, K. N. Maher, L. Ouyang, C. L. Yu, H. Park, J. Park, *Nano Lett.* **2008**, *8*, 4552.
- [24] D. Yu, J. Wu, Q. Gu, H. Park, *J. Am. Chem. Soc.* **2006**, *128*, 8148.
- [25] H. Eshet, R. Baer, D. Neuhauser, E. Rabani, *J. Phys. Chem. Lett.* **2014**, *5*, 2580.
- [26] H. Ding, N. Pan, C. Ma, Y. Wu, J. Li, H. Cai, K. Zhang, G. Zhang, W. Ren, J. Li, Y. Luo, X. Wang, J. G. Hou, *Adv. Mater.* **2014**, *26*, 3035.
- [27] W. Zhou, X. Dai, T.-M. Fu, C. Xie, J. Liu, C. M. Lieber, *Nano Lett.* **2014**, *14*, 1614.
- [28] Z. Jiang, Q. Qing, P. Xie, R. Gao, C. M. Lieber, *Nano Lett.* **2012**, *12*, 1711.
- [29] K. T. Delaney, P. Rinke, C. G. Van de Walle, *Appl. Phys. Lett.* **2009**, *94*, 191109.
- [30] X. Ni, X. Li, J. Lee, S. Liu, V. Avrutin, Ü. Özgür, H. Morkoç, A. Matulionis, *J. Appl. Phys.* **2010**, *108*, 033112.
- [31] K.-G. Gan, C.-K. Sun, S. P. DenBaars, J. E. Bowers, *Appl. Phys. Lett.* **2004**, *84*, 4675.
- [32] M. Müller, A. Paarmann, R. Ernstorfer, *Nat. Commun.* **2014**, *5*, 5292.
- [33] M. Bernardi, D. Vigil-Fowler, C. S. Ong, J. B. Neaton, S. G. Louie, *Proc. Natl. Acad. Sci. USA* **2015**, *112*, 5291.
- [34] C. Hahn, Z. Zhang, A. Fu, C. H. Wu, Y. J. Hwang, D. J. Gargas, P. Yang, *ACS Nano* **2011**, *5*, 3970.
- [35] W. Guo, M. Zhang, A. Banerjee, P. Bhattacharya, *Nano Lett.* **2010**, *10*, 3355.
- [36] F. Qian, Y. Li, S. Gradecak, H.-G. Park, Y. Dong, Y. Ding, Z. L. Wang, C. M. Lieber, *Nat. Mater.* **2008**, *7*, 701.
- [37] Y. Dong, B. Tian, T. J. Kempa, C. M. Lieber, *Nano Lett.* **2009**, *9*, 2183.
- [38] T. Kuykendall, P. Ulrich, S. Aloni, P. Yang, *Nat. Mater.* **2007**, *6*, 951.
- [39] A. David, M. J. Grundmann, *Appl. Phys. Lett.* **2010**, *96*, 103504.
- [40] S. Hammersley, D. Watson-Parris, P. Dawson, M. J. Godfrey, T. J. Badcock, M. J. Kappers, C. McAleese, R. A. Oliver, C. J. Humphreys, *J. Appl. Phys.* **2012**, *111*, 083512.
- [41] C. H. Wang, S. P. Chang, W. T. Chang, J. C. Li, Y. S. Lu, Z. Y. Li, H. C. Yang, H. C. Kuo, T. C. Lu, S. C. Wang, *Appl. Phys. Lett.* **2010**, *97*, 181101.
- [42] F. Bertazzi, M. Goano, E. Bellotti, *Appl. Phys. Lett.* **2010**, *97*, 231118.
- [43] E. Kioupakis, P. Rinke, K. T. Delaney, C. G. Van de Walle, *Appl. Phys. Lett.* **2011**, *98*, 161107.
- [44] E. Bellotti, F. Bertazzi, M. Goano, *J. Appl. Phys.* **2007**, *101*, 123706.
- [45] J. Iveland, L. Martinelli, J. Peretti, J. S. Speck, C. Weisbuch, *Phys. Rev. Lett.* **2013**, *110*, 177406.
- [46] C. X. Wang, K. Tsubaki, N. Kobayashi, T. Makimoto, N. Maeda, *Appl. Phys. Lett.* **2004**, *84*, 2313.
- [47] L. Hsu, R. E. Jones, S. X. Li, K. M. Yu, W. Walukiewicz, *J. Appl. Phys.* **2007**, *102*, 073705.
- [48] Z. Guo, J. S. Manser, Y. Wan, P. V. Kamat, L. Huang, *Nat. Commun.* **2015**, *6*, 7471.
- [49] C. Zhao, T. K. Ng, A. Prabaswara, M. Conroy, S. Jahangir, T. Frost, J. O'Connell, J. D. Holmes, P. J. Parbrook, P. Bhattacharya, B. S. Ooi, *Nanoscale* **2015**, *7*, 16658.
- [50] S. Nakamura, *Science* **1998**, *281*, 956.
- [51] M. Takashi, Y. Motokazu, N. Shuji, *Jpn. J. Appl. Phys.* **1999**, *38*, 3976.
- [52] S. Nakamura, *Semicond. Sci. Technol.* **1999**, *14*, R27.
- [53] P. Kivisaari, J. Oksanen, J. Tulkki, *Appl. Phys. Lett.* **2013**, *103*, 031103.
- [54] L. Reimer, *Scanning Electron Microscopy*, 2nd ed., Springer Series in Optical Sciences, Vol. 45, Springer, Heidelberg, Germany 1998.
- [55] S. Nakamura, M. Senoh, S. Nagahama, N. Iwasa, T. Yamada, T. Matsushita, Y. Sugimoto, H. Kiyoku, *Appl. Phys. Lett.* **1996**, *69*, 1568.
- [56] H. P. T. Nguyen, M. Djavid, S. Y. Woo, X. Liu, A. T. Connie, S. Sadaf, Q. Wang, G. A. Botton, I. Shih, Z. Mi, *Sci. Rep.* **2015**, *5*, 7744.
- [57] T. Li, A. M. Fischer, Q. Y. Wei, F. A. Ponce, T. Detchprohm, C. Wetzel, *Appl. Phys. Lett.* **2010**, *96*, 031906.
- [58] E. S. Jeon, V. Kozlov, Y. K. Song, A. Vertikov, M. Kuball, A. V. Nurmikko, H. Liu, C. Chen, R. S. Kern, C. P. Kuo, M. G. Crawford, *Appl. Phys. Lett.* **1996**, *69*, 4194.
- [59] J. Sun, A. Adhikari, B. S. Shaheen, H. Yang, O. F. Mohammed, *J. Phys. Chem. Lett.* **2016**, *7*, 985.
- [60] J. I. Khan, A. Adhikari, J. Sun, D. Priante, R. Bose, B. S. Shaheen, T. K. Ng, C. Zhao, O. M. Bakr, B. S. Ooi, O. F. Mohammed, *Small* **2016**, DOI:10.1002/smll.201503651.